Materials Chemistry and Physics 246 (2020) 122834

Contents lists available at ScienceDirect

Materials Chemistry and Physics

journal homepage: www.elsevier.com/locate/matchemphys

Particle dispersion and lattice distortion induced magnetic behavior of $La_{1-x}Sr_xMnO_3$ perovskite nanoparticles grown by salt-assisted solid-state synthesis

Jose-Luis Ortiz-Quiñonez, Lorena García-González, Francisco Enrique Cancino-Gordillo, Umapada Pal [*,1]

Instituto de Física, Benemérita Universidad Autónoma de Puebla, Apdo. Postal J-48, Puebla Pue, 72570, Mexico

HIGHLIGHTS

- $La_{1-x}Sr_xMnO_3$ perovskite nanoparticles of 90–255 nm av. Size range were fabricated by ball-milling.
- Presence of Na^+ ion at surface promotes the dispersion of $LaMnO_{3+\delta}$ nanoparticles.
- Particle dispersion modifies the T_{irr} of $La_{1-x}Sr_xMnO_3$ nanostructures.
- Substitution of La^{3+} by Sr^{2+} in $La_{1-x}Sr_xMnO_3$ increases their T_{Curie} and M_s.
- Jahn-Teller distortion and La^{3+} vacancy induced Mn^{3+} oxidation affect their magnetic behavior.

GRAPHICAL ABSTRACT

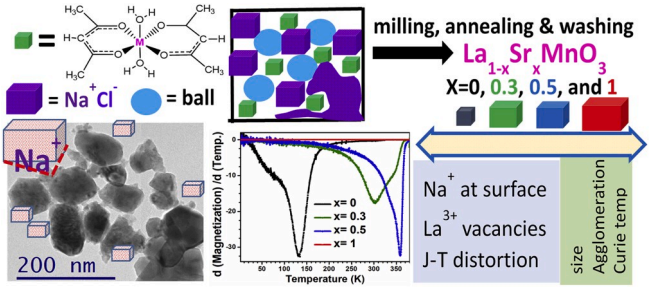

ARTICLE INFO

Keywords:
$La_{0.7}Sr_{0.3}MnO_3$ particles
Mechanosynthesis
Perovskite structure
Lanthanum manganites
Magnetic properties

ABSTRACT

$La_{1-x}Sr_xMnO_3$ perovskites are of enormous current interest due to their superior magnetoresistance and application as cathode material for solid oxide fuel cells. However, practical applications of these perovskites critically depend on size, composition, and concentration of La^{3+} vacancies at their surfaces. Here we present the fabrication of size controlled (90–255 nm average size), highly crystalline $La_{1-x}Sr_xMnO_3$ (x = 0, 0.3, 0.5, and 1) nanoparticles, simply by ball-milling of metal acetylacetonate precursors in NaCl and subsequent air-annealing. The size of the nanoparticles increased in the order $LaMnO_{3+\delta} < La_{0.7}Sr_{0.3}MnO_3 \approx La_{0.5}Sr_{0.5}MnO_3 < SrMnO_3$. While $LaMnO_{3+\delta}$ particles remain well dispersed, a fraction of particles containing Sr remains partially interconnected after air-annealing (900 °C). A change in site symmetry of the Mn^{3+}-O_6 octahedron promoted by the Jahn-Teller distortion of $LaMnO_{3+\delta}$ lattice was detected. Substitution of La^{3+} ions by Sr^{2+} increases the ferromagnetic interaction in $La_{1-x}Sr_xMnO_3$ (x = 0, 0.3, 0.5) nanostructures, increasing their Curie temperature and magnetization (M_s) progressively. Effect of particle dispersion due to Sr^{2+} incorporation on the lattice and magnetic behavior of the nanostructures is discussed considering the Jahn-Teller distortion and La^{3+} vacancy induced Mn^{3+} ion oxidation (to Mn^{4+}) in the lattice.

* Corresponding author.
E-mail address: upal@ifuap.buap.mx (U. Pal).
[1] Presently at: The Korea Centre for Artificia Photosyntheis and Department of Chemistry, Sogang University, Seoul, Republic of Korea.

https://doi.org/10.1016/j.matchemphys.2020.122834
Received 27 September 2019; Received in revised form 19 January 2020; Accepted 18 February 2020
Available online 19 February 2020

1. Introduction

$La_{1-x}Sr_xMnO_3$ is an interesting perovskite material, which manifests colossal magnetoresistance (CMR) induced by the "double-exchange" mechanism, and low field magnetoresistance (LFMR) properties [1–6]. The LFMR behavior of $La_{1-x}Sr_xMnO_3$ was seen to be further enhanced in its metal oxide composites such as $La_{1-x}Sr_xMnO_3$:CuO, CeO_2, Mn_3O_4, NiO, and MgO [5]. While $La_{1-x}Sr_xMnO_3$ nanoparticles have been utilized as catalysts for CO oxidation [7,8], NO oxidation and reduction [9], electrochemical oxygen reduction [10–12], and photocatalytic water oxidation [13], single crystalline $La_{0.5}Sr_{0.5}MnO_3$ particles of micrometric dimension have been utilized as effective cathode material in solid oxide fuel cells (SOFCs) [12]. On the other hand, $La_{1-x}Sr_xMnO_3$ nanostructures have been tested effective in hyperthermia applications for tumor therapy [14–16]. The catalytic and magnetic applications of $La_{1-x}Sr_xMnO_3$ nanoparticles are seen to depend strongly on the ratio of lanthanum and strontium ions in their lattice structure, especially at their surfaces [13,17–21].

$La_{1-x}Sr_xMnO_3$ has a distorted ABO_3-type perovskite structure for x = 0.0, 0.3 and 1.0. On the other hand, it is cubic for x = 0.5 [22]. While for x = 0.23–0.6 it manifests ferromagnetic behavior at room temperature, for the x values lower than 0.23, it behaves as insulator with paramagnetic ordering [23]. In perovskite lattice, the A cations remain in dodecahedral coordination, and the B cations stay in octahedral coordination with oxygen anions (Fig. 1). A few specific compositons of the perovskite such as $La_{0.7}Sr_{0.3}MnO_3$ and $La_{0.5}Sr_{0.5}MnO_3$ have been utilized for optoelectronic applications [24]. Mn^{4+}/Mn^{3+} ratio in them was seen to play a critical role in their magnetic and electrical properties. In fact, the Mn^{4+}/Mn^{3+} ratio determines the charge carrier concentration, and hence the viability of optoelectronic applications of these manganites [25]. On the other hand, the observed colossal magnetoresistance (CMR) in $La_{1-x}Sr_xMnO_3$ thin films is governed by the displacement of Mn^{3+} cations out of the center of the Mn^{3+}-O_6 polyhedron due to Janh-Teller effect. It should be recalled that the number of unpaired electrons in the 3d orbitals of Mn^{3+} and Mn^{4+} cations are 4 and 3, respectively. Therefore, controlling Mn^{4+}/Mn^{3+} ratio at the surface of these manganites is a key factor, which determines their technological applications.

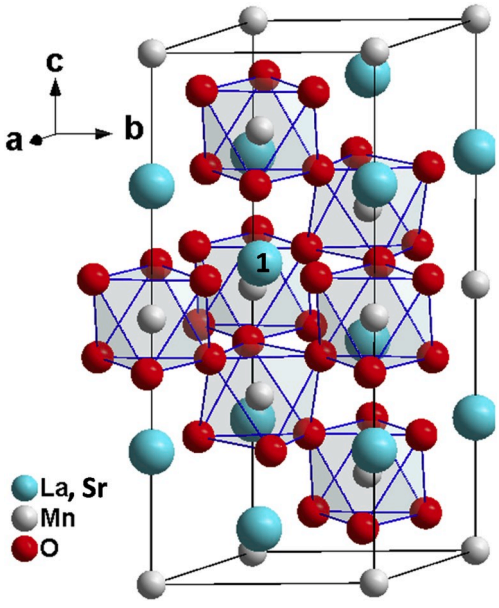

Fig. 1. Schematic representation of the lattice structure of $La_{0.7}Sr_{0.3}MnO_3$ perovskite (hexagonal unit cell). Data for the atomic positions were taken from Ref. [1]. The La/Sr cation labeled by 1 allows seeing the nearest oxygen atoms in the neighboring gray octahedra. Note that all the neighboring octahedra share only one oxygen atom.

Nanostructures such as nanoparticles and nanorods of $La_{1-x}Sr_xMnO_3$ have been synthesized earlier using solid-state such as mechanochemical synthesis [26], and chemical methods such as sol-gel [27], hydro- and solvothermal [10,11,28], etc. However, in most of the cases, the obtained nanostructures are of non-homogeneous size with poor dispersion [15,17,25,29–36], A considerable improvement in size dispersion has been accomplished by using a molten salt such as KNO_3 [37], $NaNO_3$ and KNO_3 mixture as solvent and/or the addition of organic capping agents [22]. On the other hand, strongly ionic salts such as NaCl and KCl have been utilized as dispersing medium in the mechanochemical synthesis of metal-organic framework (MOF) nanostructures [38] and nanodiamonds [39]. The use of these solid ionic solvents has been seen effective for controlling both the morphology and porosity of the nanostructures, along with improving their dispersion. For example, the presence of NaCl during high temperature (900 °C) sintering of ceria (CeO_2) nanoparticles was seen to avoid their aggregation [40].

Use of a strongly ionic salt such as NaCl in the synthesis of manganite nanostructures involving high temperature thermal annealing for inducing crystallinity has several other advantages besides acting as a dispersion medium: (i) Due to the high thermal stability of NaCl (melting point ~ 800.7 °C), it avoids the aggregation of the formed nanoparticles; (ii) Above 800 °C NaCl is a molten salt, which can work as an ionic liquid solvent, facilitating high-temperature diffusion of La^{3+}, Sr^{2+}, $Mn^{3+,4+}$ and O^{2-} ions, avoiding the formation of point defects in $La_{1-x}Sr_xMnO_3$ nanoparticles due to nonuniform cation distribution; (iii) As the Shannon ionic radius of the Na^+ ion (1.18 Å) is close to the ionic radii of Sr^{2+} (1.26 Å) and La^{3+} (1.16 Å) [41], a partial substitution of La^{3+} and Sr^{2+} cations at the surface of the $La_{1-x}Sr_xMnO_3$ particles might occur, which can modify the concentration of oxygen vacancies at their surfaces, modifying their reactivity/catalytic activity; and (iv) Since $La_{1-x}Sr_xMnO_3$ particles can oxidize CO and NO molecules [7,8,42], Cl^- ions from the molten NaCl might also be oxidized at the surface of $La_{1-x}Sr_xMnO_3$ at high temperature. In other words, $La_{1-x}Sr_xMnO_3$ particles can oxidize the Cl^- ions to Cl_2(g), avoiding the formation of undesired chloride-based impurities.

In this article, we present the fabrication of well-dispersed $La_{1-x}Sr_xMnO_3$ nanoparticles containing different mol fractions of La and Sr by ball-milling, utilizing NaCl as dispersing medium and metal acetylacetonate complexes as precursors. Effects of NaCl use on particle size, particle aggregation, structural distortion, and magnetic behavior of the perovskite nanostructures have been studied extensively. X-ray diffraction (XRD), scanning electron microscopy (SEM), and transmission electron microscopy (TEM) were utilized for structural and morphological characterization of the nanostructures. MicroRaman and X-ray photoelectron spectroscopy (XPS) were utilized for determining the structural phase and chemical bonding of elements in the nanoparticles. Vibrating sample magnetometry (VSM) was performed to study the magnetic behavior of the perovskite nanostructures.

2. Experimental

2.1. Materials

Manganese nitrate tetrahydrate ($Mn(NO_3)_2•4H_2O$, >97.0%), lanthanum nitrate hexahydrate ($La(NO_3)_3•6H_2O$, 99.99%), strontium nitrate ($Sr(NO_3)_2$, 99+%) and acetylacetone ($C_5H_8O_2$, >99.5%) were purchased from Sigma-Aldrich, Mexico. Sodium hydroxide (NaOH, 98.15%) was purchased from J.T. Baker, Mexico. Sodium chloride (NaCl, >99%) was purchased from Omnichem, Mexico. Deionized (DI) water from a Millipore system (ρ > 18.2 M Ω•cm) was utilized for washing the fabricated nanostructures.

2.2. Synthesis of metal acetylacetonates

Metal acetylacetonate complexes (Mn (acac)$_2$, La (acac)$_3$ and Sr (acac)$_2$) were synthesized through co-precipitation, as reported by Nforna et al., [31]. For the synthesis of Mn (acac)$_2$, first, a solution of sodium acetylacetonate was prepared as precipitating agent by dropwise addition of stoichiometric amount (15 mL) of acetylacetone to a NaOH solution (5.82 g of NaOH in 60 mL of water) at 50 °C under magnetic stirring for 20 min. A precursor solution of Mn was prepared by dissolving 48.49 mmol of $Mn(NO_3)_2 \bullet 4H_2O$ in 50 mL of DI water under magnetic stirring. After that, the hot solution of sodium acetylacetonate was slowly added to the precursor solution of Mn and kept at this temperature for 30 min under magnetic stirring. The product of the reaction was a pale-yellow precipitate of manganese acetylacetonate, (Mn (acac)$_2$). The precipitate was cooled down to room temperature, filtered by suction in a Büchner funnel, washed four times with DI water, and vacuum dried for 12 h. This process was repeated for La $(NO_3)_3 \bullet 6H_2O$ and $Sr(NO_3)_2$ to obtain a white precipitate of lanthanum acetylacetonate and a white-pearl precipitate of strontium acetylacetonate.

2.3. Synthesis of $La_{1-x}Sr_xMnO_3$ nanoparticles

$La_{1-x}Sr_xMnO_3$ nanoparticles were prepared by thermal decomposition of metal acetylacetonates of Mn, La and Sr in presence of sodium chloride under high energy ball milling. The nominal x values utilized for the synthesis of $La_{1-x}Sr_xMnO_3$ were 0.0, 0.3, 0.5 and 1.0. In a typical synthesis, for example, in the case of $La_{0.7}Sr_{0.3}MnO_3$, 0.5783 g of Mn (acac)$_2$, 0.6863 g of La (acac)$_3$, and 0.1823 g of Sr (acac)$_2$ were mixed with 7.234 g of NaCl. The w/w ratio {Mn (acac)$_2$ + La (acac)$_3$ + Sr (acac)$_2$}/NaCl was 1:5. The metal acetylacetonates and sodium chloride mixture was then placed inside a 100 mL agate milling jar filled with 32 agate gridding balls (10 mm diameter). Then the jar was set up in a planetary ball mill (PQ-N2 Gear Drive 4) station, and the milling was performed for 24 h at 200 rpm. The obtained fine powder was then transferred to an alumina crucible and air-annealed inside a Carbolite tubular furnace at 750 °C for 6 h, heating the sample at 5 °C/min rate. After cooling down to room temperature, the product was washed in 1.0 L of DI water to remove NaCl used as dispersing material. After washing, the product was separated by decantation. The obtained precipitate was re-dispersed in 500 mL of DI water, ultrasonicated for 2 min, and recovered by centrifugation. This step was repeated for 4 times. Finally, the obtained product was dried at 70 °C for 5 h. To induce crystallization, the obtained powder sample was subjected to another thermal annealing carried out at 900 °C for 5 h in air, with a heating rate of 5 °C/min. A similar procedure was followed for the synthesis of $La_{1-x}Sr_xMnO_3$ with x = 0.0, 0.5 and 1.0.

2.4. Characterization of $La_{1-x}Sr_xMnO_3$ nanoparticles

To analyze the crystallinity and phase structure, powder XRD patterns of the samples were recorded in a Bruker D8 diffractometer, utilizing CuKα (λ = 1.5406 Å) radiation. The spectra were recorded at 0.02°/step with a scan rate of 0.2 s/step in the 2θ range of 20 − 80°. For morphology and composition analysis, a small amount of each of the powder samples was dispersed in ethanol and deposited over clean Si wafer. The samples were inspected in a JEOL JSM-7800 F field-emission scanning electron microscope (FE-SEM) coupled with an Oxford Instrument X-Max energy dispersive spectrometer (EDS). Vibrational characteristics of nanostructures were analyzed by Raman spectroscopy at room temperature. A Horiba LabRamHR system equipped with a 633 nm He–Ne laser and a thermoelectrically cooled charge-coupled device (CCD) detector was utilized for recording the Raman spectra of the samples. MicroRaman spectra of the samples were acquired using appropriate objective lenses and filters (neutral density filters) to avoid their laser-induced (due to the high intensity of the exciting laser beam) burning. The nanostructures were analyzed further by recording their low- and high-resolution transmission electron microscopy (TEM) images in a JEOL 2100 F transmission electron microscope, operating at 200 kV accelerating voltage. The samples for TEM analysis were prepared by drop-casting their colloidal suspension (in ethanol) over carbon-coated copper grids. For the analysis of composition and chemical states of constituting elements, X-ray photoelectrons spectra (XPS) of the samples were recorded in a Thermo Scientific spectrometer with Al Kα (1486.6 eV) radiation source. Deconvolution of the core-level emission bands was performed using Pseudo-Voight2 functions with 70% Gaussian and 30% Lorentzian components, after subtracting Shirley type backgrounds. Magnetic properties of the nanostructures were studied by recording their magnetization (M − H) curves and magnetization under zero-field cooling (ZFC) and applied field cooling (FC) curves in a DynaCool physical property measurement system (PPMS, DynaCool, Quantum Design).

3. Results and discussion

3.1. X ray diffraction

Room temperature XRD patterns of the fabricated $La_{1-x}Sr_xMnO_3$ nanoparticles are presented in Fig. 2. Rietveld refinement of the XRD patterns of the $La_{1-x}Sr_xMnO_3$ samples and corresponding cell parameters are included in Fig. S1 (Supporting Information). All the samples revealed well-resolved diffraction peaks of single phase. Position and relative intensity of the diffraction peaks of the $LaMnO_{3+\delta}$ (x = 0.0) and $La_{0.7}Sr_{0.3}MnO_3$ (x = 0.3) samples correspond well to their rhombohedral perovskite phase of space group $R\bar{3}c$ (PDF # 04-012-5560 and 00-056-0616, respectively). The structure with space group $R\bar{3}c$ was derived from the simple-cubic perovskite ($Pm\bar{3}m$) lattice by rotation of adjacent MnO_6 octahedra in opposite direction around the $[111]_c$ (cubic) axis [43].

Stoichiometric (with no oxygen excess, i.e. δ = 0.0), and low oxygen excess (δ ≤ 0.07) $LaMnO_{3+\delta}$ perovskites have orthorhombic unit cells of *Pbnm* space group. However, for δ ≥ 0.09, they contain rhombohedral unit cells (space group $R\bar{3}c$) [44,45]. The unit cell volumes for δ = 0.9, 0.10, 0.11, 0.12, 0.13, and 0.14 are reported to be of 118.9, 118.25, 117.63, 117.92, 117.44, 117.18 Å^3, respectively [44]. The volume of the rhombohedral unit cell for $LaMnO_{3+\delta}$ obtained in the present work is 116.78 Å^3 (lattice parameters a = 5.462 Å and α = 60.59°), which is slightly lower than the value determined by Töpfer and Goodenough

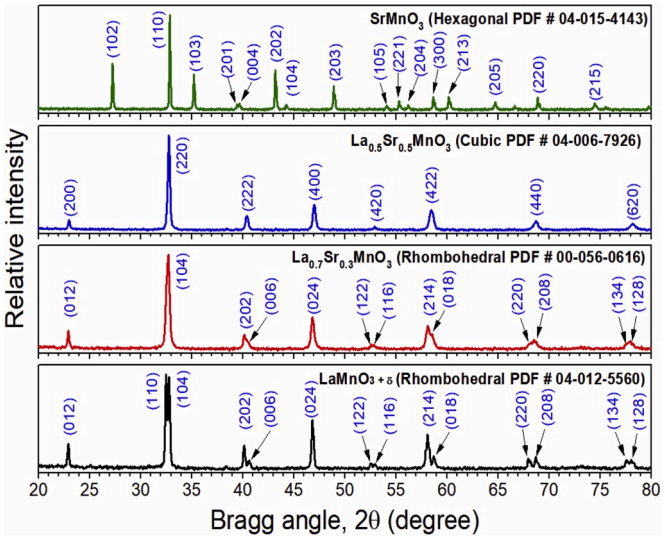

Fig. 2. Room temperature XRD patterns of the $La_{1-x}Sr_xMnO_3$ samples annealed at 900 °C.

(cell volume = 117.18 Å^3, a = 5.469 Å, α = 60.58°) for $LaMnO_{3+\delta}$ with δ = 0.14. The oxygen excess (δ) in $LaMnO_{3+\delta}$ has been demonstrated in previous studies using neutron diffraction by other authors [45–49]. The lower unit cell volume (and also the d values) estimated for the $LaMnO_{3+\delta}$ nanostructures fabricated in this work is probably due to the formation of metal ion vacancies in them. The formation of one La^{3+} vacancy in the perovskite lattice induces the transformation of three Mn^{3+} ions into Mn^{4+} cations to maintain its charge neutrality. As the ionic radius of Mn^{4+} ion is smaller than the ionic radius of Mn^{3+}, the observed change in unit cell volume of the perovskite unit cell is probably also caused by the oxidation of Mn^{3+} cations.

On the other hand, the positions of the diffraction peaks revealed for the $La_{0.5}Sr_{0.5}MnO_3$ (x = 0.5) sample are in good agreement with its pseudo-cubic perovskite structure, with space group $Fm\bar{3}m$ (PDF # 04-006-7926). Finally, the diffraction pattern of the $SrMnO_3$ sample matches well with its four-layered hexagonal phase (PDF # 04-015-4143; space group $P6_3/mmc$), which is the most stable phase of $SrMnO_3$ below 1308 K [50]. To explain the change in the type of unit cell with increase in x value, the Goldschmidt tolerance factor (τ) for the $La_{1-x}Sr_xMnO_3$ perovskites was estimated. The τ value is important because it determines whether the structure of the perovskite is rhombohedral (0.8< τ < 0.89), cubic (0.89< τ < 1.0), or hexagonal (1.0< τ < 1.13) [51]. The τ values estimated for the perovskite nanostructures correspond to x values 0.0, 0.3, 0.5 and 1.0 were 0.844, 0.878, 0.934, and 0.982, respectively (see Tables S1 and S2, Supporting Information). Appearance of well-resolved diffraction bands of high intensity in all the samples indicate their good crystallinity after annealing at 900 °C for 5 h. To highlight the effect of high temperature annealing on the crystallinity of the perovskite nanostructures, we present a typical XRD pattern of the $La_{0.7}Sr_{0.3}MnO_3$ sample annealed at 750 °C in Fig. S2 (supporting information). As can be seen, while the rhombohedral phase of the perovskite was formed even at this temperature, the intensity (or the signal-to-noise ratio) of the diffraction bands is considerably low, indicating their partial crystallization at this lower annealing temperature.

3.2. Scanning electron microscopy (SEM)

Typical SEM images of the $La_{1-x}Sr_xMnO_3$ samples are presented in Fig. 3. Formation of quasi-spherical particles in 30 to a few hundred nanometer size range is very clear in the micrographs. The particles appear partially fused and interconnected. As can be observed in the size distribution histograms presented as insets, the size of the particles in lanthanum containing samples remained in between 30 and 225 nm, while the size of the particles in $SrMnO_3$ sample varies in between 100 and 550 nm. The average size of the particles increased from 89.6 ± 26 to 128.8 ± 39 nm with the increase of Sr mole fraction from x = 0.0 to x = 0.5. In fact, the estimated average size of the $SrMnO_3$ (x = 1.0) particles is considerably larger (255 ± 87 nm) than in other samples. The average crystallite size in the manganites containing Sr mole fractions x = 0.0, 0.3, and 0.5 estimated from the Rietveld refinement of their XRD spectra were 111, 110, and 124 nm, respectively, which are in accordance with the particle size values estimated from their SEM images. The narrowest diffraction peaks for the $SrMnO_3$ sample agree very well with the largest particle size (255 ± 87 nm) found in its SEM images. The results indicate the particle size in the perovskite nanostructures is controlled by the Sr mole fraction in them.

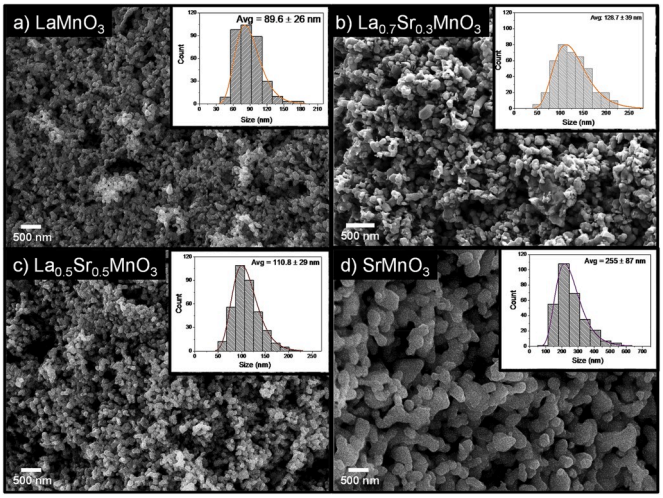

Fig. 3. Typical SEM images of $La_{1-x}Sr_xMnO_3$ samples prepared with nominal x values of (a) 0.0, (b) 0.3 (c) 0.5 and (d) 1.0. Corresponding particle size distribution histograms with their log-normal fits are presented as insets.

Typical EDS spectra for the $La_{1-x}Sr_xMnO_3$ samples are shown in Fig. S3 (supporting information). The EDS estimated elemental composition of the $La_{1-x}Sr_xMnO_3$ samples presented in Table 1 demonstrates a gradual increase of Sr content in the nanostructures with the increase of its nominal content in the reaction mixture. As can be observed in Table 1, all samples revealed their oxygen excess. Also, a subtle atomic percentage of Na could be detected in all the samples. The amount of Na in $LaMnO_{3+\delta}$ sample is about five times larger than in the other three samples. However, presence of chlorine was not detected in the nanostructures, which confirms the absence of NaCl in the samples. EDS estimated Sr/(Sr + La) ratios in the samples remained very close to their nominal values, indicating adequate incorporation of Sr in the particle lattice. Although the (La + Sr)/Mn ratio in all the samples should be 1.0, it was seen to be a bit higher for $LaMnO_{3+\delta}$ (1.11), which decreased progressively (Table 1) with the increase of Sr content in the samples.

3.3. Transmission electron microscopy (TEM)

Typical TEM images of the $La_{1-x}Sr_xMnO_3$ samples are shown in Fig. 4. As can be noticed from Figs. 4a and S4 (supporting information), the majority of the $LaMnO_{3+\delta}$ particles remain dispersed without fusing after high-temperature thermal annealing. Similarly (Figs. 4c and S5), most of the $La_{0.5}Sr_{0.5}MnO_3$ nanoparticles remained dispersed after the thermal treatment. The average particle sizes determined from the TEM images (considering more than 80 particles of each sample) of the samples are 52 ± 17 and 88 ± 29 nm (Fig. S6, supporting information) for the $LaMnO_{3+\delta}$ and $La_{0.5}Sr_{0.5}MnO_3$ samples, respectively.

On the other hand, the HRTEM images of the $LaMnO_{3+\delta}$ particles revealed their high crystallinity (see the red square in Fig. 5). Presence of La vacancy sites in the crystal lattice of the particles can be noticed (marked by yellow arrows) in the HRTEM image enclosed by the blue square in Fig. 5. Interplanar distances (d) determined for this defective particle are 3.82, 3.18 and 2.19 Å, which correspond well both to the (012), (103), and (006) planes of $LaMnO_{3+\delta}$ and (211), (122) and (411) planes of Mn_2O_3. Therefore, this particle could either correspond to $LaMnO_{3+\delta}$ with several vacancies induced by the partial substitution of La^{3+} with Na^+ cations, or an impurity of Mn_2O_3 phase. $LaMnO_3$ with cation vacancies is usually referred to as $LaMnO_{3+\delta}$. In this regard, Zakhvalinskiĭ et al. prepared $LaMnO_{3+\delta}$ (δ = 0.065, 0.100, 0.112, 0.125, 0.133, 0.140, and 0.154) particles and claimed the presence of cation

Table 1
EDS estimated elemental composition of the $La_{1-x}Sr_xMnO_3$ particles.

Sample	Na (at %)	Mn (at%)	Sr (at %)	La (at %)	O (at %)	Sr/(Sr + La)	(La + Sr)/Mn
$LaMnO_3$	1.79	14.44	–	16.00	67.75	0.00	1.11
$La_{0.7}Sr_{0.3}MnO_3$	0.41	16.24	4.90	13.22	65.24	0.27	1.12
$La_{0.5}Sr_{0.5}MnO_3$	0.14	17.63	7.80	10.29	64.15	0.43	1.03
$SrMnO_3$	0.13	17.66	18.06	–	64.15	1.00	1.02

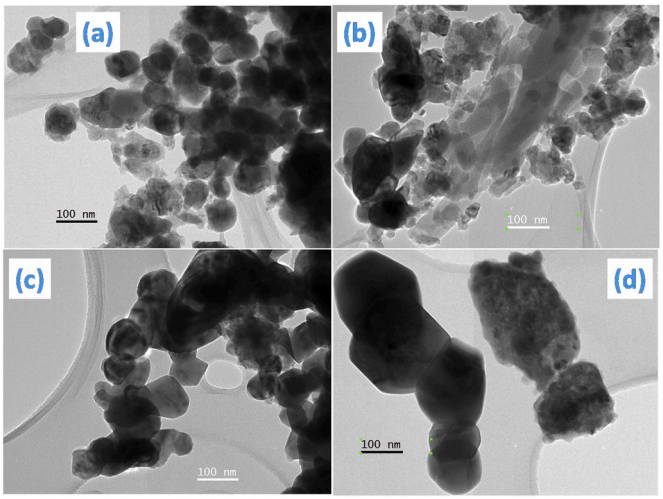

Fig. 4. Typical TEM images of $La_{1-x}Sr_xMnO_3$ samples prepared with nominal x values of (a) 0.0, (b) 0.3 (c) 0.5 and (d) 1.0.

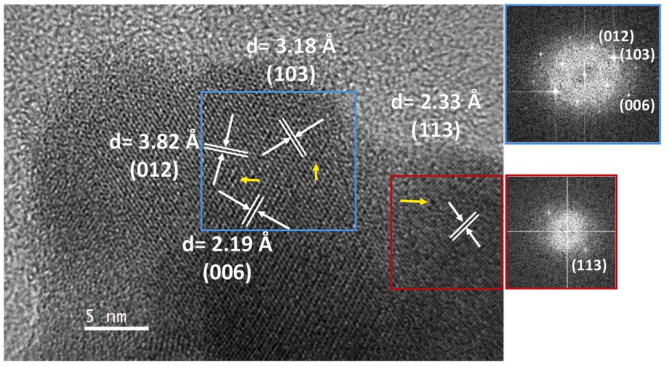

Fig. 5. A typical high resolution TEM (HRTEM) image of the $LaMnO_{3+\delta}$ particles. Interplanar distances (*d*) and corresponding lattice planes are shown. Cation vacancies in the lattice are shown by yellow arrows. The spot patterns correspond to the fast Fourier transform (FFT) of the two zones highlighted with blue and red squares in the image. (For interpretation of the references to color in this figure legend, the reader is referred to the Web version of this article.)

vacancies in the samples [26]. While rhombohedral $LaMnO_{3+\delta}$ particles with $\delta = 0.12–0.15$ [52], 0.13–0.18 [44], and 0.15–0.26 [53] have been fabricated by several other research groups, they either did not consider or could not detect the formation of cation vacancy in the perovskite lattice through HRTEM imaging [17,54–56]. Although the formation of cation vacancy in $LaMnO_{3+}\delta$ and (La, M)$MnO_{3+}\delta$ (where M = Na, Ca) and its effect on the magnetic behavior of the perovskites have been discussed by Horyn et al. [57], and Malavasi et al. [46], they did not provide any direct evidence such as HRTEM images of the perovskites demonstrating the formation of cation vacancies in their lattice. While the incorporation of Na^+ ions in the fabricated nanostructures is very clear from their EDS analysis (Table 1), the formation of Na^+ ion doping-induced La^{3+} vacancies in $LaMnO_{3+\delta}$ lattice is also clear in the HRTEM image of the sample presented in Fig. 5.

However, due to large particle size (>100 nm) of the $La_{1-x}Sr_xMnO_3$ perovskites with x = 0.3, 0.5 and 1.0, it was not possible to acquire their HRTEM images (difficult for the electron beam to pass through these large particles).

3.4. Raman spectroscopy

As the lattice distortion and possible presence of impurities in solid samples can be detected from their Raman spectra, we performed Raman spectroscopy of the fabricated particles at room temperature (Fig. 6). The Raman spectrum of $LaMnO_{3+\delta}$ revealed the presence of two broad bands located at 512 and 640 cm^{-1} (Fig. 6), corresponding to out-of-phase O–Mn–O bending vibration and in-phase stretching vibration of Mn–O in the MnO_6 octahedron, respectively [58]. Appearance of broad Raman bands for the $LaMnO_{3+\delta}$ nanoparticles confirms the lattice distortion discussed in the XRD section. These results agree well with the reported Raman features of $LaMnO_{3+\delta}$ obtained using crossed polarization of the incident and scattered beams [43]. Also, the intensity of these bands depends on the degree of the Jahn-Teller distortion in Mn^{3+}-O_6 octahedra. As the Sr content in $La_{1-x}Sr_xMnO_3$ (x = 0, 0.3, and 0.5) increases, the extent of Jahn-Teller distortion decreases, diminishing the intensity of these Raman bands [43,59]. Moreover, due to defect-induced lattice perturbation, the bands become broader [58].

To explain the differences in the degree of the Jahn-Teller distortion in the perovskites, we should consider that the electron configurations of Mn^{3+} and Mn^{4+} cations in $La_{1-x}Sr_xMnO_3$ are high-spin d^4 and high-spin d^3, respectively. While the energy of 3d electrons in Mn^{3+} cations can be decreased through Jahn-Teller effect by forming a geometrically distorted octahedron, it does not occur for Mn^{4+} cations. The ground state of Mn^{3+} cation in the Mn^{3+}-O_6 octahedron is electronically degenerated, and an extension or compression of Mn^{3+}-O^{2-} bond pair along the z axis breaks the degeneracy of these states. In other words, the presence of Mn^{3+} cations decreases the site symmetry form O_h to D_{4h}, and the Mn^{3+}-O^{2-} bond distances along the z axis become larger than the ones in the xy plane. The driving force for this change in site symmetry is the decrease in the global energy of the solid.

On the other hand, group theory analysis predicts eight Raman active phonons for the perovskites with hexagonal symmetry [60], such as $SrMnO_3$. The Raman spectrum of $SrMnO_3$ (x = 1.0) sample presented in Fig. 6 shows 3 bands, peaked around 342, 431 and 642 cm^{-1}, which have been ascribed to one phonon processes related to Mn displacements inside the Mn^{4+}-O_6 octahedral tilting (E_{1g}), octahedral asymmetric

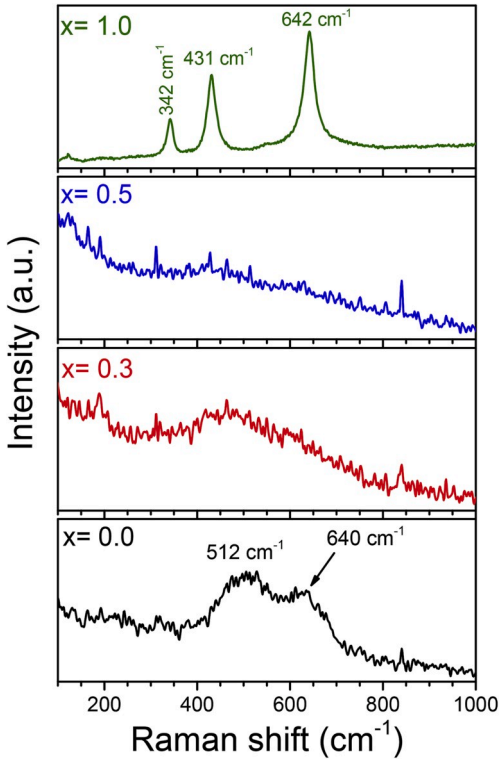

Fig. 6. Raman spectra of $La_{1-x}Sr_xMnO_3$ samples prepared with different nominal x values.

stretching (E_{2g}), and symmetric stretching (A_{1g}), respectively [60]. It must be noticed that the Raman spectrum of the $SrMnO_3$ nanoparticles strongly differs from the Raman spectra of rest of the samples (x = 0.0, 0.3 and 0.5), since $SrMnO_3$ (x = 1.0) belongs to different space group, and its structure is Mn^{4+} centered, which does not produce Jahn-Teller-distorted octahedral [43,59]. From XRD analysis, it is clear that incorporation of Sr in $La_{1-x}Sr_xMnO_3$ nanoparticles generates nanostructures with different unit cells (rhombohedral, cubic and hexagonal) due to the rotation of adjacent MnO_6 octahedra in opposite direction around the [111] axis. This difference in the type of unit cell (and hence of local symmetry) is further supported by the high variation in the number and width of the Raman peaks observed for each sample.

3.5. X-ray photoelectron spectroscopy (XPS)

XPS survey spectra of the $La_{1-x}Sr_xMnO_3$ perovskites are presented in Fig. 7. As expected, we could detect only the emissions corresponding to La, Sr, Mn and O elements in the samples, along with the signal of adventitious carbon. In addition, traces of Na associated to remaining of NaCl were detected in all the samples. Orbitals associated to the main emission peaks in the XPS spectra are indicated in Fig. 7. Aüger lines located at 494, 900, 973, and 1226 eV correspond to Na ($KL_{23}L_{23}$), Mn ($L_3M_{23}M_{45}$), O ($KL_{23}L_{23}$), and C (KVV) elements (see blue arrows in Fig. 7), respectively [61]. However, no emission associated with chlorine was observed in the samples, which should appear around 199 and 201 eV binding energies for the Cl $2p_{3/2}$ and Cl $2p_{1/2}$ orbitals, respectively. Elimination of chlorine ions from the samples occurred due to the significant change in the standard reduction potential (E°) of the Cl_2/Cl^- couple at high annealing temperature, 900 °C (see Supporting Information).

Normalized high-resolution XPS spectra for selected orbital are depicted in Fig. 8. Binding energies (BEs) of the La $3d_{3/2}$ and La $3d_{5/2}$ orbitals in $La_{1-x}Sr_xMnO_3$ perovskites were estimated to be 850.29 and 833.54 eV, respectively (Fig. 8a). The La $3d_{5/2}$ orbital revealed a satellite peak located at 837.56 eV. No detectable shift in the position of these peaks was observed due to progressive substitution of La ions by Sr ions. However, for $LaMnO_3$ (x = 0), the band correspond to La $3d_{5/2}$ orbital (appeared in-between 833.67 and 836.01 eV) is more intense than its intensity in the remaining manganites. This difference might be due to the presence of La–OH bonds at the surface of $LaMnO_{3+\delta}$. Since the Sr^{2+} ($pka = 13.3$), La^{3+} ($pka = 8.5$) and $Mn^{3+,4+}$ ($pka < 5$) ions are classified as very weakly acidic, weakly acidic, and moderately acidic cations, respectively [62], formation of -La-OH species can occur at the surface of $LaMnO_3$ by H_2O hydrolysis.

High-resolution XPS spectra of Mn $2p_{3/2}$ and Mn $2p_{1/2}$ orbitals in the $La_{1-x}Sr_xMnO_3$ perovskites are presented in Fig. 8b. The binding energy position of the Mn $2p_{3/2}$ orbital at 640.92 eV in $LaMnO_{3+\delta}$ indicates the Mn cations in the sample remain both in 3+ and 4+ oxidation states (the 4+ oxidation state preserves the charge electroneutrality around La^{3+} vacancies and Na^+ substitutions). However, on substitution of La^{3+} cations by Sr^{2+} cations, the peak position of the Mn $2p_{1/2}$ emission gradually shifted to higher binding energies. A right (low energy) shoulder around 640.44 eV appeared for the $La_{0.7}Sr_{0.3}MnO_3$ and $La_{0.5}Sr_{0.5}MnO_3$ samples due to the presence of Mn^{3+} cations, in addition to the Mn^{4+} cations. For the $SrMnO_3$ sample, in which the oxidation state of all the Mn cations is 4+, the Mn $2p_{3/2}$ peak is centered at higher BE, i.e. at 641.67 eV.

It should be noted that while the FWHM (full width at high maximum) of the Mn $2p_{3/2}$ emission from the lanthanum (La) containing perovskites is about 3.47 eV, it is only about 2.3 eV for the $SrMnO_3$ perovskite. Such a drastic difference in the FWHM value of Mn $2p_{3/2}$ orbitals between the La containing and La free perovskites is the result of: (i) presence of both Mn^{3+} and Mn^{4+} cations in the same phase, and (ii) Jahn-Teller effect (i.e. the two Mn–O bonds along the z axis are longer than the four Mn–O bonds in the xy plane). Overlapping of orbitals is weaker in longer Mn–O bonds than in shorter Mn–O bonds,

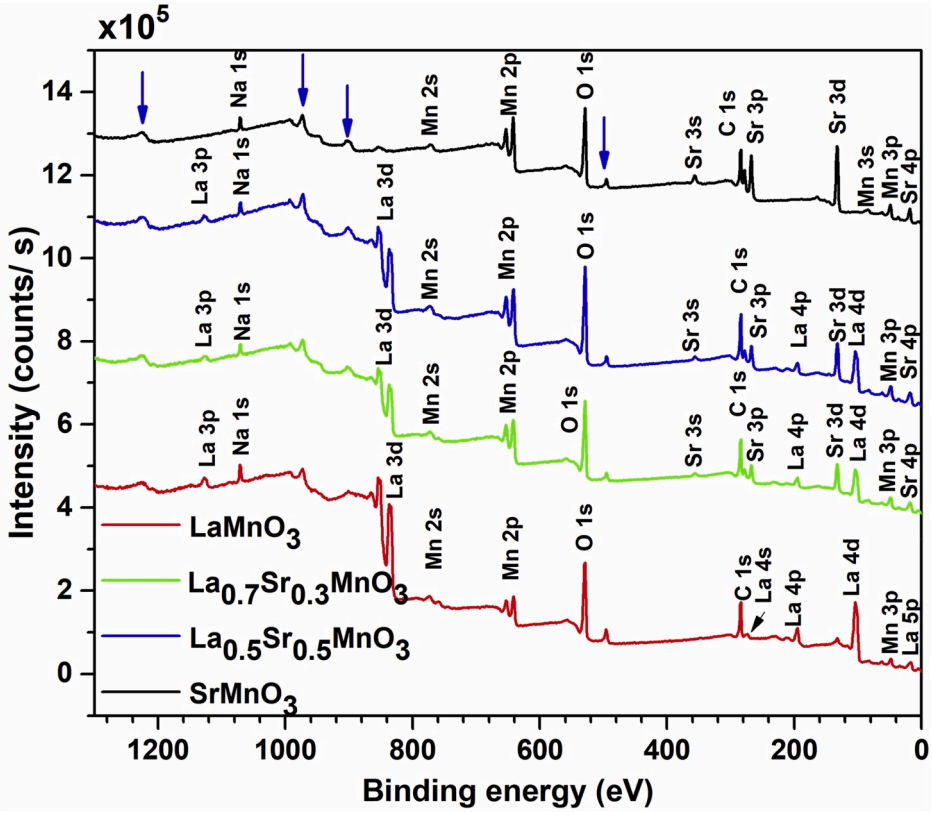

Fig. 7. XPS survey spectra of $La_{1-x}Sr_xMnO_3$ perovskites with x = 0, 0.3, 0.5, and 1.0.

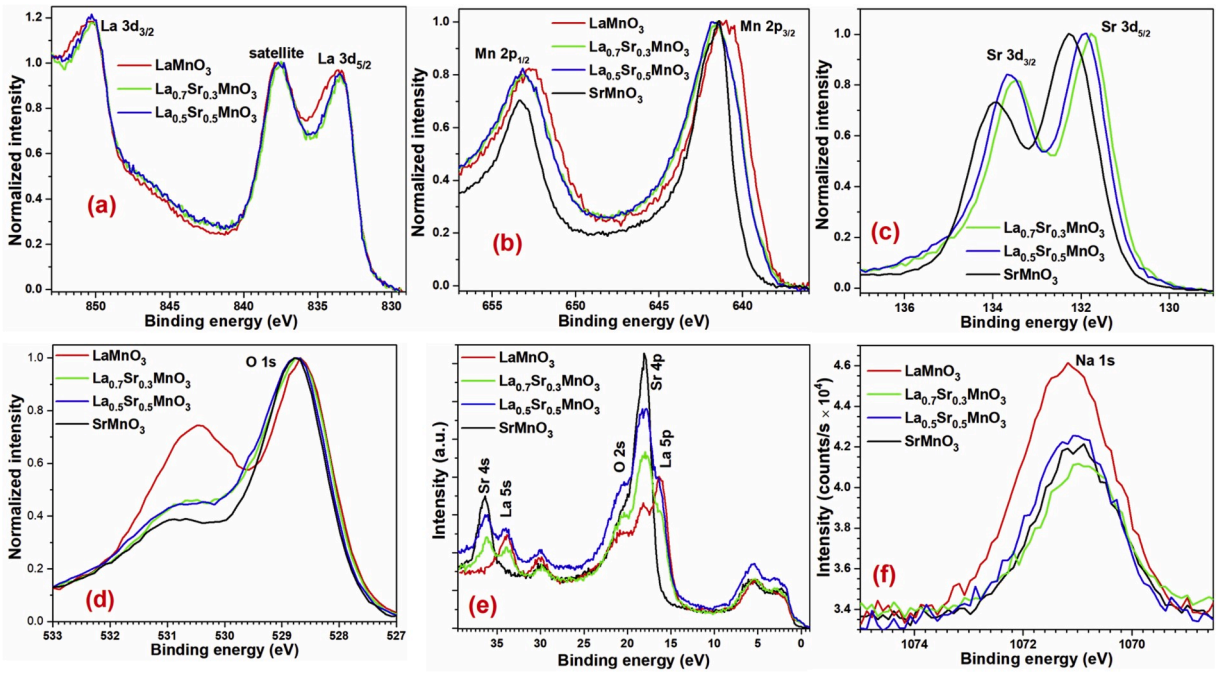

Fig. 8. High-resolution of XPS spectra of $La_{1-x}Sr_xMnO_3$ perovskites with x = 0.0, 0.3 0.5, and 1.0. (a) La $3d_{3/2}$ and La $3d_{5/2}$, (b) Mn $3p_{1/2}$ and Mn $3p_{3/2}$, (c) Sr $3d_{3/2}$ and Sr $3d_{5/2}$, (d) O 1s, (e) O 2s, Sr 4p, La 5p; and (f) Na 1s.

affecting the BE of Mn $2p_{3/2}$ orbital. As a result, the Mn $2p_{3/2}$ emission band is broader in $LaMnO_3$, $La_{0.7}Sr_{0.3}MnO_3$, and $La_{0.5}Sr_{0.5}MnO_3$ than in $SrMnO_3$ (see Fig. 8b). As has been discussed in section 3.4, there is no Jahn-Teller effect in the $SrMnO_3$ phase. Since the Jahn-Teller effect plays a key role in the colossal magnetoresistance exhibited by $La_{0.7}Sr_{0.3}MnO_3$ below a certain critical temperature [63], it is worth to highlight the differences in the FWHM of the Mn $2p_{3/2}$ emission bands in their XPS spectra of the perovskites (Fig. 8b).

There exists another contribution to the observed difference in the FWHM values. The La^{3+} cations in $LaMnO_{3+\delta}$ are coordinated by 12 O^{2-} anions with varied La–O bond distances (i.e. 2.418, 2.46, 2.579, 2.65, 2.72, 3.156, 3.189, 3.35 Å) [64]. Consequently, the electron density around the oxygen anions in the La–O bonds are different; which also affects the BE of the Mn $2p_{3/2}$ orbital in the perovskites. On the contrary, in $SrMnO_3$ the twelve Sr–O bond distances are very similar (2.73, 2.73, 2.76 and 2.85 Å) [65]. Likewise, the Mn–O bond distances in $SrMnO_3$ are very close (1.87 and 1.89 Å) [65], and therefore the BEs of the Mn $2p_{3/2}$ emission bands are similar, making its XPS emission sharper.

Fig. 8c shows the core-level XPS spectra of Sr $3d_{3/2}$ and Sr $3d_{5/2}$ orbitals for the $La_{1-x}Sr_xMnO_3$ perovskites. The Sr $3d_{5/2}$ (Sr $3d_{3/2}$) peaks for the $La_{0.7}Sr_{0.3}MnO_3$, $La_{0.5}Sr_{0.5}MnO_3$, and $SrMnO_3$ perovskites are centered at 131.76 (133.49), 131.92 (133.60), and 132.25 (133.91) eV, respectively. As can be observed, the BE of electrons in the Sr $3d_{5/2}$ and Sr $3d_{3/2}$ orbitals shift gradually towards lower energy with the incorporation of La. It should be noted further that while in $SrMnO_3$ there are Sr–O–Mn^{4+} moieties, in $La_{0.5}Sr_{0.5}MnO_3$ and $La_{0.7}Sr_{0.3}MnO_3$, there are both Sr–O–Mn^{3+} and Sr–O–Mn^{4+} moieties. As the Mn^{4+} cation has a larger electron-withdrawing capacity from Sr atoms than the Mn^{3+} cations, the BEs of the Sr $3d_{5/2}$ and Sr $3d_{3/2}$ orbitals shift gradually towards higher energy with the increase of Sr content.

The O1s orbital emissions from $LaMnO_{3+\delta}$ and $SrMnO_3$ are centered at 528.68 and 528.77 eV, respectively (Fig. 8d). This difference makes sense since the reported BE for the O 1s orbital for the La_2O_3 and SrO are 528.8 and 530.3 eV, respectively [66]. Deconvolution of the O 1s emission bands is depicted in Fig. S7 (supporting information). The areas of the fitted component bands (fit peaks) are included in Table S3 (supporting information). In the spectrum of $LaMnO_{3+\delta}$ there is a second peak centered at 530.47 eV (with a shoulder at 529.87 eV), which is associated to surface hydroxyl groups, such as –LaOOH or -Mn-OH bonded to the surface of this manganite (see the fit peaks in green color in Fig. S7). The intensity ratios of the components associated to the M – OH and M-O-M (M = Sr^{2+}, La^{3+}, and $Mn^{3+,4+}$) bonds for the $LaMnO_3$, $La_{0.7}Sr_{0.3}MnO_3$, $La_{0.7}Sr_{0.3}MnO_3$, and $SrMnO_3$ were estimated to be 0.87, 0.40, 0.33, and 0.37, respectively. Zhi et al. [12], used powder $La_{0.5}Sr_{0.5}MnO_3$ samples and microtubes in electrochemical oxygen reduction at operating temperatures between 700 and 900 °C, obtaining M-OH/(M-O-M) ratios of 0.97 for the powder and 1.32 for microtubes [12]. Therefore, the presence of O 1s peak at 530.5 eV in the core-level XPS spectra of our $La_{1-x}Sr_xMnO_3$ samples indicates the occurrence of reduction-oxidation reactions at the surface of the manganites.

Presence of –OH groups at the surface of $La_{1-x}Sr_xMnO_3$ perovskite samples exposed to water agrees with the observations made by Stoerzinger et al. for their humidity exposed $La_{1-x}Sr_xMnO_3$ samples [11]. In fact, generation of M – OH groups at the surface of $La_{0.6}Sr_{0.4}MnO_3$ thin films has been demonstrated by Li et al. by treating them in oxidizing mixture (5H_2O, 1 NH_4OH, 1H_2O_2) [67]. Furthermore, the formation of LaOOH bonds at the surface of $LaCoO_3$ causing a splitting of the O 1s band has also been observed by Natile et al. [68], and Stoerzinger et al., [69]. An emission band around 532 eV attributed to physisorbed H_2O molecule was detected in all the samples (see the red component in Fig. S7).

As can be seen in Fig. 8e, the Sr 4p, O 2s, and La 5p orbitals overlap due to closeness of binding energies. This finding is interesting because atomic orbitals of same (or closer) binding energies (and proper symmetry) usually form strong chemical bonds, and consequently, increase the thermal stability of the oxides. Reported theoretical calculations of the density of states (DOS) for the $La_{0.7}Sr_{0.3}MnO_3$ perovskite indicate that the DOS for the Sr 4p and La 5p orbitals are located at −15.0 and −16.0 eV, respectively [70]. However, the XPS spectra presented in Fig. 8e indicate the DOS for the Sr 4p and La 5p orbitals are located at −18.09 and −16.31 eV, respectively.

As can be noticed in Fig. 8f, and the surface elemental compositions of $La_{1-x}Sr_xMnO_3$ samples presented in Table 2, all the samples contain Na^+ cations, with the highest atomic percentage in $LaMnO_{3+\delta}$ sample. The higher XPS estimated atom % of Na (Table 2) in the samples in comparison to their EDS estimated values (Table 1), clearly indicates the

Table 2
XPS estimated elemental composition at the surface of $La_{1-x}Sr_xMnO_3$ nanoparticles.

Sample	Na (at%)	Mn (at%)	Sr (at%)	La (at%)	O (at%)
$LaMnO_3$	12.13	15.59	–	8.05	64.23
$La_{0.7}Sr_{0.3}MnO_3$	5.26	17.62	18.64	3.14	55.33
$La_{0.5}Sr_{0.5}MnO_3$	5.14	16.67	22.26	3.13	52.78
$SrMnO_3$	4.82	17.88	30.62	–	46.69

Na^+ cations are incorporated mainly at the surface of the manganites, bonding with surface oxygen atoms.

3.6. Magnetic properties

Since the magnetic moment per unit mass (emu/g) is a tool to find structural changes in magnetic materials, we recorded the magnetization vs applied magnetic field (M − H) curves of the synthesized $La_{1-x}Sr_xMnO_3$ nanostructures (Fig. 9). As can be noticed in Fig. 9, non-stoichiometric lanthanum manganite ($LaMnO_{3+\delta}$) nanoparticles exhibit paramagnetic behavior at 300 K. However, at lower temperatures they adopt a ferromagnetic (FM) phase with saturation magnetization (M_s) of 59.54 emu/g at 1.8 K (Fig. 9b). La^{3+} vacancies present in the $LaMnO_{3+\delta}$ nanoparticles transform some of the Mn^{3+} ions into Mn^{4+} cations to maintain the charge neutrality of the $LaMnO_{3+\delta}$ lattice (Fig. 10). According to the double-exchange mechanism proposed by Zener [71], the Mn^{3+}-O-Mn^{4+} moieties in $LaMnO_{3+\delta}$ adopt FM order below the Curie temperature (T_C), while the Mn^{3+}-O-Mn^{3+} moieties adopt an antiferromagnetic (AFM) order. Interestingly, the *Ms* value (59.54 emu/g at 1.8 K) we detected for the $LaMnO_{3+\delta}$ nanoparticles is very similar to the value found in nanofiber composed of 20 nm $LaMnO_{3+\delta}$ grains (65.0 emu/g) [72], larger than that of 18 nm (45.0 emu/g) and 35 nm (~42.0 emu/g) $LaMnO_{3+\delta}$ nanoparticles [73,74], but smaller than 55 nm $LaMnO_{3+\delta}$ nanoparticles (75.0 emu/g) [74].

Presence of stoichiometric $LaMnO_3$ in the sample fabricated in this study was rule out as stoichiometric $LaMnO_3$ adopts an orthorhombic lattice structure (instead of rhombohedral observed in the present study) and presents AFM ordering [45,75] For the sake of reference, reported M_s value for $LaMnO_3$ single-crystal is 12.5 emu/g in the easy direction of magnetization at 2 K at 5 T applied magnetic field [76].

On the other hand, $La_{0.7}Sr_{0.3}MnO_3$ perovskites revealed a mixed superparamagnetic (SP) - paramagnetic behavior at 300 K with M_s value of about 26 emu/g (Fig. 9b). At 1.8 K, the value of M_s increased up to 56.90 emu/g. This value at 1.8 K is similar to the value reported for $La_{0.7}Sr_{0.3}MnO_3$ nanoparticles [16,22,37], but about 30 and 23 emu/g lower than that of microspheres [77], and small nanoparticles with well-connected grain boundaries (i.e. particles containing fused grains) [1], respectively. The *Ms* value at 1.8 K estimated for the $La_{0.7}Sr_{0.3}MnO_3$ nanoparticles fabricated in the present work is in good accordance with their well-dispersed (not fused, see Fig. 3b) characteristic.

The $La_{0.5}Sr_{0.5}MnO_3$ nanostructures revealed their SP ordering at 300 K with a M_s value about 29.59 emu/g. However, at 200 K, they exhibited a FM ordering, with M_s and H_c values of 41.87 emu/g and 31.0 Oe, respectively (Fig. 9a and b & S8). A comparison of the M_s values of the $La_{1-x}Sr_xMnO_3$ nanostructures displayed at different temperatures (Fig. 9b) indicates that the fabricated $La_{0.5}Sr_{0.5}MnO_3$ nanostructures are best suited for utilization in room-temperature magnetic hyperthermia.

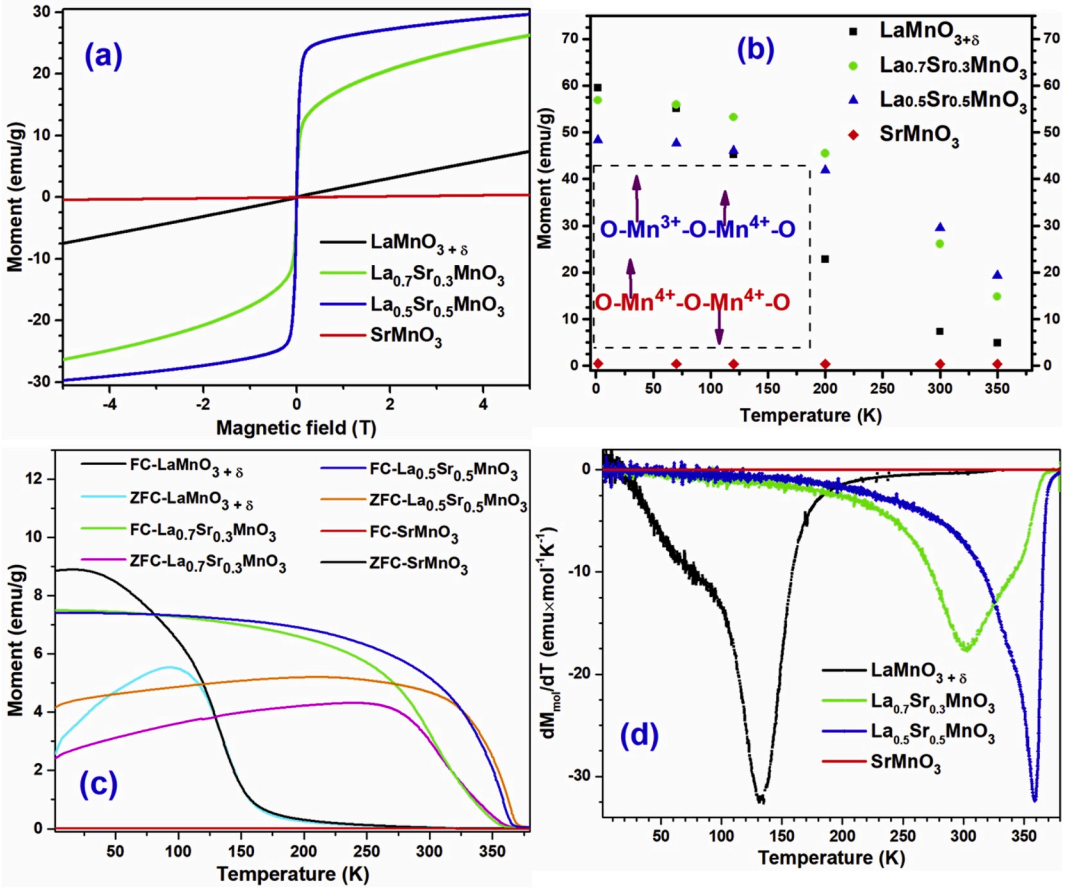

Fig. 9. Magnetic behaviors of the $La_{1-x}Sr_xMnO_3$ perovskites: (a) Magnetization (M) vs applied magnetic field (H) curves recorded at 300 K; (b) Saturation magnetization (M_s) measured at 5 T at different temperatures; inset shows the relative magnitude and alignment of the atomic magnetic moments in Mn^{3+} and Mn^{4+} cations; (c) Zero-field cooling (ZFC) and field cooling (FC) curves measured at 100 Oe; (d) Temperature variation of the first derivative of molar magnetization (M_{mol}) for the $La_{1-x}Sr_xMnO_3$ perovskites with different x values.

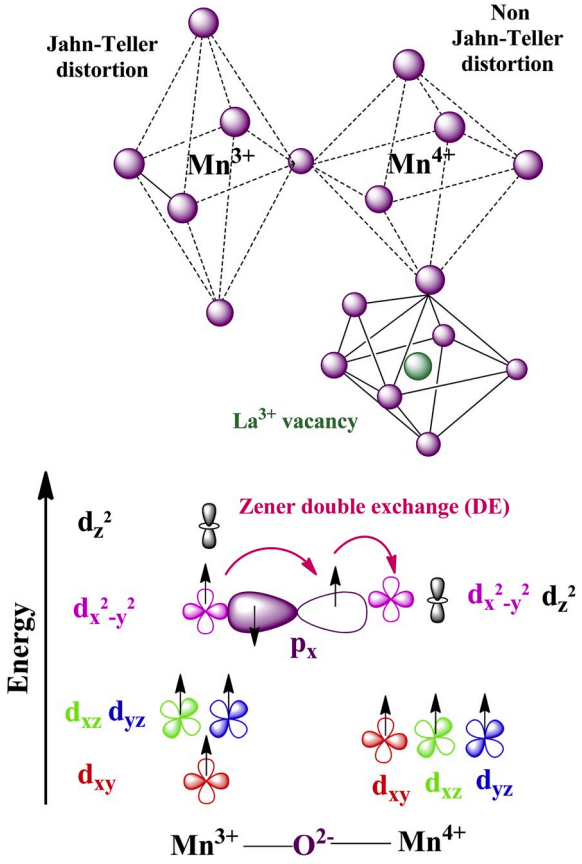

Fig. 10. (Top) Schematic representation of the geometric distortion of Mn^{3+}-O_6 octahedron in $LaMnO_{3+\delta}$ perovskite lattice due to Jahn-Teller (J–T) effect. J-T distortion does not occur in Mn^{4+}-O_6 octahedron. The green sphere inside the polyhedron represents a La^{3+} vacancy. The La^{3+} vacancy transforms some neighboring Mn^{3+} cations into Mn^{4+} cations. (Bottom) Schematics of the relative energy positions of the 3d orbitals in Mn^{3+} and Mn^{4+} cations (five orbitals for each cation) present in the $La_{1-x}Sr_xMnO_3$ (x = 0, 0.3 and 0.5) perovskites; orbital in purple color represents the $2p_x$ orbital of the O^{2-} anion in Mn^{3+}-O-Mn^{4+} moiety. Black arrows in each orbital indicate the spin of the electrons. Note that the spin alignment corresponds to a ferromagnetic material (provided that the temperature is below its Curie temperature). Pink arrows show the double electron exchange (DE) responsible for the magnetoresistance under an external magnetic field.

Finally, the $SrMnO_3$ nanostructures exhibited an antiferromagnetic (AFM) behavior at all the temperatures (Fig. 9a & b), as expected for a solid composed of Mn^{4+}-O-Mn^{4+} moieties, in which there is no possibility of occurring the double exchange (DE) interaction phenomenon.

The zero-field cooling (ZFC) and field cooling (FC) curves (2 K/min) for the $La_{1-x}Sr_xMnO_3$ perovskites recorded applying 100 Oe magnetic field are shown in Fig. 9c. A paramagnetic to ferromagnetic transition around 130 K can be clearly observed for the $LaMnO_{3+\delta}$ nanostructures, which explains the large increase in magnetic moment (Fig. 9b) below this temperature. Irreversibility temperature (T_{irr}, the point at which the ZFC and FC curves bifurcate) for the $LaMnO_{3+\delta}$ sample (around 130 K) is close to its reported Curie temperature (T_c= 135 K) [78]. T_{irr} for the $LaMnO_{3+\delta}$, $La_{0.7}Sr_{0.3}MnO_3$, and $La_{0.7}Sr_{0.3}MnO_3$ phases are 125, 318, and 325 K, respectively (Fig. 9c). As can be seen in Table 3, the T_{irr} for $LaMnO_{3+\delta}$ nanoparticles fabricated in the present work is considerably lower than the values reported in the literature. The lower T_{irr} value of the nanoparticles might be associated to their non-aggregated (particles are not fused) arrangement. However, estimated T_{irr} values for the $La_{0.7}Sr_{0.3}MnO_3$ nanoparticles fabricated in the present study are close to the values reported for dispersed nanoparticles (see Table 3). Notably, the FC and ZFC curves of the sample cross at the T_{irr}, instead of merging.

Table 3
Irreversibility temperature (T_{irr}) for the $LaMnO_{3+\delta}$ and $La_{0.7}Sr_{0.3}MnO_3$ nanoparticles in comparison to their values reported in the literature. The ZFC and FC curves were recorded under 100 Oe applied magnetic field.

Phase	Particle size (nm)	Aggregation behavior	T_{irr} (K)	Refefernce
$LaMnO_{3+\delta}$	52	Highly dispersed nanoparticles	125	**Present work**
$LaMnO_{3+\delta}$	18	(a)	220	[73]
$LaMnO_{3+\delta}$	–	(a)	230	[84]
$LaMnO_{3+\delta}$	20	Fused grains forming nanofibers.	240	[72]
$LaMnO_{3+\delta}$	40	Fused nanoparticles.	255	[74]
$La_{0.7}Sr_{0.3}MnO_3$	25	(a)	275 (b)	[37]
$La_{0.7}Sr_{0.3}MnO_3$	50	Highly fused nanoparticles.	300 (c)	[85]
$La_{0.7}Sr_{0.3}MnO_3$	20	Highly fused nanoparticles.	300	[1]
$La_{0.7}Sr_{0.3}MnO_3$	25	Dispersed nanoparticles functionalized with betaine hydrochloride	325	[15]
$La_{0.7}Sr_{0.3}MnO_3$	129	Dispersed nanoparticles	290 (d)	**Present work**
$La_{0.7}Sr_{0.3}MnO_3$	129	Dispersed nanoparticles	318	**Present work**
$La_{0.7}Sr_{0.3}MnO_3$	129	Dispersed nanoparticles	336 (e)	**Present work**
$La_{0.5}Sr_{0.5}MnO_3$	–	(a)	300	[84]
$La_{0.5}Sr_{0.5}MnO_3$	88	Dispersed nanoparticles	325	**Present work**

(a) TEM images were not included in the reference. ZFC and FC curves were measured at (b) 200 Oe, (c) 10 Oe, (d) 200 Oe and (e) 50 Oe.

Such a crossing/inversion between the ZFC and FC curves has been observed in $Tb(Co_{0.94}Fe_{0.06})_2$ [79], $CoFe_2O_4$ [80], $La_{0.275}Pr_{0.35}Ca_{0.375}MnO_3$ [81], $NiFe_2O_4$ [82], and graphene oxide/$NiFe_2O_4$ composite [83]. Such anomaly in magnetic behavior of the nanostructures has been attributed to their large magnetostriction [80,81], presence of a frustrated spin system [83], or a spin-glass-like surface disorder [82].

Broadening of the Mn $3p_{3/2}$ XPS peaks (Fig. 8b) and high saturation magnetization (Fig. 9b) in the $La_{1-x}Sr_xMnO_3$ perovskite (x = 0, 0.3 and 0.5) can be obtained only if both the Mn^{3+} and M^{4+} ions are present in the perovskite. Therefore, the use of XPS and vibrating sample magnetometry (VSM) techniques in combination is important, as they help to confirm the presence of Mn cations in mixed valence states in the perovskites. Besides, for $LaMnO_{3+\delta}$, both the high M-OH/M-O-M (M = Sr^{2+}, La^{3+}, and $Mn^{3+,4+}$) ratio found through XPS analysis and the low T_{irr} value determined from the FC/ZFC curves support the claim that the $LaMnO_{3+\delta}$ nanoparticles have small size and are not aggregated.

The temperature of the transition from paramagnetic to ferromagnetic, T_c, could be estimated from the maximum of the first derivative of molar magnetization (M_{mol}) with respect to temperature (Fig. 9d). The T_c values obtained for the $La_{1-x}Sr_xMnO_3$ nanoparticles with x = 0, 0.3 and 0.5 were 133, 303, and 358 K, respectively. Such a gradual increase in T_c value with the increase of strontium mole fraction in the perovskites can be understood considering its dependence on the interionic spin interaction of nearest-neighbors. The interaction between localized spins of the neighboring ions are treated by a perturbation theory in which the spin-dependent resonance integrals for parallel coupling of spins are:

$$t_{ij} \approx \varepsilon_\sigma \lambda_\sigma^2 cos\varphi \cos\left(\frac{\theta_{ij}}{2}\right) \quad (1)$$

where ε_σ is the stabilization energy of the band formed by the $Mn^{3+,4+}$ d^{22}_{x-y} and O $2p_x$ orbitals (see Fig. 10), λ_σ is the overlap integral between atomic orbitals, $(180^\circ - \varphi)$ is the angle in the Mn–O–Mn bond, and θ_{ij} is the angle between the spins on neighboring Mn cations [46,86]. In other words, t_{ij} is a measure of the strength of the ferromagnetic Mn^{3+}-O-Mn^{4+} interactions in perovskites.

The higher T_c observed (Fig. 9d) for the $La_{0.5}Sr_{0.5}MnO_3$ sample can be attributed to the higher ferromagnetic interaction, caused by the following two factors: (i) Since the reported Mn–O–Mn angle in $La_{0.5}Sr_{0.5}MnO_3$ is 180° but only 164° in $La_{0.7}Sr_{0.3}MnO_3$ [84], $cos\varphi$ in eq. (1) is 1 for $La_{0.5}Sr_{0.5}MnO_3$ and 0.96 for $La_{0.7}Sr_{0.3}MnO_3$. (ii) The radius of Mn^{4+} cation is smaller than the radius Mn^{3+} cation, and also the $La_{0.5}Sr_{0.5}MnO_3$ has higher Mn^{4+} content than $La_{0.7}Sr_{0.3}MnO_3$. The smaller size of Mn^{4+} generates a greater overlapping of orbitals (λ_σ) of the Mn^{4+} and oxygen ions, increasing the value of t_{ij} in eq. (1). The results presented in this article clearly demonstrate that the size and aggregation determine the T_{irr} and M_S value of $LaMnO_{3+\delta}$ nanoparticles. While the use of common salt in solid-state mechano-synthesis of $La_{1-x}Sr_xMnO_3$ nanoparticles helps to increase their dispersion, substitution of La^{3+} ions by Sr^{2+} ions induces changes in the Mn–O–Mn angle and Mn^{3+}/Mn^{4+} ratio, which affect the magnetic behavior (M_s, T_{irr}, *and* T_c values) of the perovskite nanoparticles.

4. Conclusions

Quasi-spherical $La_{1-x}Sr_xMnO_3$ (x = 0, 0.3, 0.5, and 1) nanoparticles of 90–255 nm average sizes could be synthesized through solvent-free ball milling process utilizing NaCl as a dispersing medium, and subsequent thermal annealing. While the Cl^- ions of the used NaCl (as dispersing agent) escape during high temperature (900 °C) air-annealing, the Na^+ ions remain at the surface of the perovskite particles preventing their aggregation. The poor dispersion of $SrMnO_3$ particles is due to lower concentration of Na^+ ions at their surface. Substitution of La^{3+} ions by Sr^{2+} causes a gradual increase in the average size of $La_{1-x}Sr_xMnO_3$ nanoparticles. It also progressively increases the ferromagnetic interaction in $La_{1-x}Sr_xMnO_3$ (x = 0, 0.3, 0.5) nanostructures, increasing their Curie temperature gradually. Incorporation of Sr not only reduces the Jahn-Teller distortion in $LaMnO_{3+\delta}$ lattice (up to x = 0.5), but also decreases the concentration of La^{3+} vacancies. Creation of La^{3+} vacancies in $LaMnO_{3+\delta}$ lattice generates Mn^{4+} ions (through oxidation of Mn^{3+} ions) to preserve the charge neutrality of the lattice, enhancing the magnetization (M_S) of the nanostructures through inter-ionic spin interaction. While the presence of Na^+ ions at the surface of $La_{1-x}Sr_xMnO_3$ nanoparticles helps to keep them disaggregated during high-temperature thermal annealing, it causes a reduction of irreversibility temperature (T_{irr}) and saturation magnetization (M_s) values of the nanostructure.

Declaration of competing interest

The authors declare that they have no known competing financial interests or personal relationships that could have appeared to influence the work reported in this paper.

Acknowledgements

FECG and JLOQ thank CONACyT, Mexico for extending doctoral (CVU # 784149) and postdoctoral (CONACyT-SENER) fellowships, respectively. Financial helps offered by VIEP-BUAP (Grant # 100236944-BUAP 2019) and CONACYT, Mexico (Grants # INFR-2014-02-23053,INFR-2011-1-163153, and A1-S-26720) are acknowledged.

Appendix A. Supplementary data

Supplementary data to this article can be found online at https://doi.org/10.1016/j.matchemphys.2020.122834.

References

[1] A. Sadhu, S. Bhattacharyya, Enhanced low-field magnetoresistance in $La_{0.71}Sr_{0.29}MnO_3$ nanoparticles synthesized by the nonaqueous sol-gel route, Chem. Mater. 26 (2014) 1702–1710, https://doi.org/10.1021/cm4041665.

[2] T. Walter, K. Dörr, K. Müller, B. Holzapfel, D. Eckert, M. Wolf, D. Schlafer, L. Schultz, R. Grotzschel, Low-field magnetoresistance of $La_{0.7}Sr_{0.3}MnO_3$ thin films with gradually changed texture, Appl. Phys. Lett. 74 (1999) 2218–2220, https://doi.org/10.1063/1.123806.

[3] Y. Tokura, A. Urushibara, Y. Moritomo, T. Arima, A. Asamitsu, G. Kido, N. Furukawa, Giant magnetotransport phenomena in filling-controlled kondo lattice system: $La_{1-x}Sr_xMnO_3$, J. Phys. Soc. Japan. 63 (1994) 3931–3935.

[4] Z.X. Cheng, H.F. Zhen, A.H. Li, X.L. Wang, H. Kimura, CMR $La_{0.7}Ca_{0.3}MnO_3$ and $La_{0.7}Sr_{0.3}MnO_3$ thin film fabricated by sol – gel method, J. Cryst. Growth 275 (2005) 2415–2419, https://doi.org/10.1016/j.jcrysgro.2004.11.351.

[5] M. Fan, H. Wang, S. Misra, B. Zhang, Z. Qi, X. Sun, J. Huang, H. Wang, Microstructure, magnetic, and magnetoresistance properties of $La_{0.7}Sr_{0.3}MnO_3$: CuO nanocomposite thin films, ACS Appl. Mater. Interfaces 10 (2018) 5779–5784, https://doi.org/10.1021/acsami.7b17398.

[6] T.D. Thanh, P.T. Phong, D.H. Manh, N. V Khien, L. V Hong, T.L. Phan, S.C. Yu, Low-field magnetoresistance in $La_{0.7}Sr_{0.3}MnO_3/BaTiO_3$ composites, J. Mater. Sci. Mater. s Electron. 24 (2013) 1389–1394, https://doi.org/10.1007/s10854-012-0943-y.

[7] K. Huang, X. Chu, W. Feng, C. Zhou, W. Si, X. Wu, L. Yuan, S. Feng, Catalytic behavior of electrospinning synthesized $La_{0.75}Sr_{0.25}MnO_3$ nanofibers in the oxidation of CO and CH_4, Chem. Eng. J. 244 (2014) 27–32, https://doi.org/10.1016/j.cej.2014.01.056.

[8] F. Teng, W. Han, S. Liang, B. Gaugeu, R. Zong, Y. Zhu, Catalytic behavior of hydrothermally synthesized $La_{0.5}Sr_{0.5}MnO_3$ single-crystal cubes in the oxidation of CO and CH_4, J. Catal. 250 (2007) 1–11, https://doi.org/10.1016/j.jcat.2007.05.007.

[9] X. Wu, L. Xu, D. Weng, The NO selective reduction on the $La_{1-x}Sr_xMnO_3$ catalysts, Catal. Today 90 (2004) 199–206, https://doi.org/10.1016/j.cattod.2004.04.027.

[10] K. Huang, L. Yuan, Yilan Jiang, J. Zhang, Z. Geng, L. Luo, S. Feng, Hydrothermal shape controllable synthesis of $La_{0.5}Sr_{0.5}MnO_3$ crystals and facet effect on electron transfer of oxygen reduction, Inorg. Chem. Front. 5 (2018) 732–738, https://doi.org/10.1039/c7qi00687j.

[11] K.A. Stoerzinger, W.T. Hong, X.R. Wang, R.R. Rao, S. Bengaluru Subramanyam, C. Li, Ariando, T. Venkatesan, Q. Liu, E.J. Crumlin, K.K. Varanasi, Y. Shao-Horn, Decreasing the hydroxylation affinity of $La_{1-x}Sr_xMnO_3$ perovskites to promote oxygen reduction electrocatalysis, Chem. Mater. 29 (2017) 9990–9997, https://doi.org/10.1021/acs.chemmater.7b03399.

[12] M. Zhi, G. Zhou, Z. Hong, J. Wang, R. Gemmen, K. Gerdes, A. Manivannan, D. Ma, N. Wu, Single crystalline $La_{0.5}Sr_{0.5}MnO_3$ microcubes as cathode of solid oxidefuel cell, Energy Environ. Sci. 4 (2011) 139–144, https://doi.org/10.1039/c0ee00300j.

[13] C. Zhou, K. Huang, L. Yuan, W. Feng, X. Chu, Z. Geng, X. Wu, L. Wang, S. Feng, Green catalyst: magnetic $La_{0.7}Sr_{0.3}MnO_3$ hollow microspheres, New J. Chem. 39 (2015) 2413–2416, https://doi.org/10.1039/c4nj01955e.

[14] N.D. Thorat, K.P. Shinde, S.H. Pawar, K.C. Barick, C.A. Betty, R.S. Ningthoujam, Polyvinyl alcohol: an efficient fuel for synthesis of superparamagnetic LSMO nanoparticles for biomedical application, Dalton Trans. 41 (2012) 3060–3071, https://doi.org/10.1039/c2dt11835a.

[15] N.D. Thorat, R.M. Patil, V.M. Khot, A.B. Salunkhe, A.I. Prasad, K.C. Barick, R. S. Ningthoujam, S.H. Pawar, Highly water-dispersible surface-functionalized LSMO nanoparticles for magnetic fluid hyperthermia application, New J. Chem. 37 (2013) 2733–2742, https://doi.org/10.1039/c3nj00007a.

[16] P.T. Phong, D.H. Manh, L.H. Nguyen, D.K. Tung, N.X. Phuc, I.J. Lee, Studies of superspin glass state and AC-losses in $La_{0.7}Sr_{0.3}MnO_3$ nanoparticles obtained by high-energy ball-milling, J. Magn. Magn Mater. 368 (2014) 240–245, https://doi.org/10.1016/j.jmmm.2014.05.025.

[17] P. Tiwari, C. Rath, Evolution of structure and magnetic properties of stoichiometry and oxygen rich $LaMnO_3$ nanoparticles, J. Magn. Magn Mater. 441 (2017) 635–641, https://doi.org/10.1016/j.jmmm.2017.06.020.

[18] A. Maignan, C. Martin, B. Vertruyen, D. Flahaut, S. H, Magnetic and electronic ground states of B-site-substituted $LaMnO_3$: from antiferromagnetism to ferromagnetism, J. Magn. Magn Mater. 280 (2004) 75–83, https://doi.org/10.1016/j.jmmm.2004.02.023.

[19] K.P. Shinde, S.S. Pawar, S.H. Pawar, Influence of annealing temperature on morphological and magnetic properties of $La_{0.9}Sr_{0.1}MnO_3$, Appl. Surf. Sci. 257 (2011) 9996–9999, https://doi.org/10.1016/j.apsusc.2011.06.126.

[20] K.P. Shinde, S.S. Pawar, P.M. Shirage, S.H. Pawar, Studies on morphological and magnetic properties of $La_{1-x}Sr_xMnO_3$, Appl. Surf. Sci. 258 (2012) 7417–7420, https://doi.org/10.1016/j.apsusc.2012.04.052.

[21] K. Huang, X. Chu, L. Yuan, W. Feng, X. Wu, X. Wang, S. Feng, Engineering the surface of perovskite $La_{0.5}Sr_{0.5}MnO_3$ for catalytic activity of CO oxidation, Chem. Commun. 50 (2014) 9200–9203, https://doi.org/10.1039/C4CC00023D.

[22] Y. Tian, D. Chen, X. Jiao, $La_{1-x}Sr_xMnO_3$ (x = 0, 0.3, 0.5, 0.7) nanoparticles nearly freestanding in water: preparation and magnetic properties, Chem. Mater. 18 (2006) 6088–6090, https://doi.org/10.1021/cm0622349.

[23] M.C. Martin, G. Shirane, Magnetism and structural distortion in the $La_{0.7}Sr_{0.3}MnO_3$ metallic ferromagnet, Phys. Rev. B 53 (1996) 285–290, https://doi.org/10.1103/PhysRevB.53.14285.

[24] Z.G. Sheng, M. Nakamura, W. Koshibae, T. Makino, Y. Tokura, M. Kawasaki, Magneto-tunable photocurrent in manganite-based heterojunctions, Nat. Commun. 5 (2014) 1–7, https://doi.org/10.1038/ncomms5584.

[25] Y. Zhou, X. Zhu, S. Li, Effect of heat treatment condition on magnetic, electrical transport and magnetoresistance properties of $La_{0.67}Sr_{0.33}MnO_3$ manganite coatings, Ceram. Int. 44 (2018) 15010–15018, https://doi.org/10.1016/j.ceramint.2018.05.130.

[26] V.S. Zakhvalinski, R. Laiho, K.G. Lisunov, E. Lähderanta, P.A. Petrenko, Y. P. Stepanov, J. Salminen, V.N. Stamov, Preparation and magnetic properties of

$LaMnO_{3+\delta}$, Phys. Solid State 48 (2006) 2300–2309, https://doi.org/10.1134/S1063783406120109.
[27] K. Navin, R. Kurchania, The effect of particle size on structural, magnetic and transport properties of $La_{0.7}Sr_{0.3}MnO_3$ nanoparticles, Ceram. Int. 44 (2018) 4973–4980, https://doi.org/10.1016/j.ceramint.2017.12.091.
[28] K. Huang, L. Yuan, Y. Jiang, J. Zhang, Z. Geng, L. Luo, S. Feng, Hydrothermal shape controllable synthesis of $La_{0.5}Sr_{0.5}MnO_3$ crystals and facet effect on electron transfer of oxygen reduction, Inorg. Chem. Front. 5 (2018) 732–738, https://doi.org/10.1039/c7qi00687j.
[29] Y.H. Huang, Z.G. Xu, C.H. Yan, Z.M. Wang, T. Zhu, C.S. Liao, S. Gao, G.X. Xu, Soft chemical synthesis and transport properties of $La_{0.7}Sr_{0.3}MnO_3$ granular perovskites, Solid State Commun. 114 (2000) 43–47, https://doi.org/10.1016/S0038-1098(99)00575-X.
[30] X. Wu, L. Xu, B. Yang, D. Weng, Surface characterization and catalytic performance of $La_{0.7}Sr_{0.3}MnO_{3+\lambda}$ coating deposited by plasma spraying, Surf. Coating. Technol. 184 (2004) 40–46, https://doi.org/10.1016/j.surfcoat.2003.10.052.
[31] E.A. Nforna, Structure and magnetic properties of lanthanum strontium ferrites nanopowders synthesized by thermal decomposition of mixed metal acetyl acetonates, Int. J. Eng. Res. Technol. 4 (2015) 907–914.
[32] M. Popa, L. Van Hong, M. Kakihana, Particle morphology characterization and magnetic properties of $LaMnO_{3+d}$ perovskites, Physica B 327 (2003) 237–240.
[33] T. Ahmad, I.H. Lone, M. Ubaidullah, K. Coolhan, Low-temperature synthesis, structural and magnetic properties of self-dopant $LaMnO_{3+\delta}$ nanoparticles from a metal-organic polymeric precursor, Mater. Res. Bull. 48 (2013) 4723–4728, https://doi.org/10.1016/j.materresbull.2013.08.007.
[34] R.S. Guo, Q.T. Wei, H.L. Li, F.H. Wang, Synthesis and properties of $La_{0.7}Sr_{0.3}MnO_3$ cathode by gel combustion, Mater. Lett. 60 (2006) 261–265, https://doi.org/10.1016/j.matlet.2005.08.027.
[35] V. Ravi, S.D. Kulkarni, V. Samuel, S.N. Kale, J. Mona, R. Rajgopal, A. Daundkar, P. S. Lahoti, R.S. Joshee, Synthesis of $La_{0.7}Sr_{0.3}MnO_3$ at 800 °C using citrate gel method, Ceram. Int. 33 (2007) 1129–1132, https://doi.org/10.1016/j.ceramint.2006.02.008.
[36] A.B. Antipov, A.N. Grigoriev, S.V. Zayats, V.V. Ivanov, A.R. Kaul, Low-field magnetoresistance of $La_{0.7}Sr_{0.3}MnO_3$ nanoceramics processed by different precursor approaches and powder compaction techniques, Mendeleev Commun. 14 (2004) 148–150, https://doi.org/10.1070/mc2004v014n04abeh001959.
[37] F. Luo, Y.H. Huang, C.H. Yan, S. Jiang, X.H. Li, Z.M. Wang, C.S. Liao, Molten alkali metal nitrate flux to well-crystallized and homogeneous $La_{0.7}Sr_{0.3}MnO_3$ nanocrystallites, J. Magn. Magn Mater. 260 (2003) 173–180, https://doi.org/10.1016/S0304-8853(02)01317-3.
[38] J. Yang, X. Feng, G. Lu, Y. Li, C. Mao, Z. Wen, W. Yuan, NaCl as a solid solvent to assist the mechanochemical synthesis and post-synthesis of hierarchical porous MOFs with high I_2 vapour uptake, Dalton Trans. 47 (2018) 5065–5071, https://doi.org/10.1039/c8dt00339d.
[39] A. Pentecost, S. Gour, V. Mochalin, I. Knoke, Y. Gogotsi, Deaggregation of nanodiamond powders using salt- and sugar-assisted milling, ACS Appl. Mater. Interfaces 2 (2010) 3289–3294, https://doi.org/10.1021/am100720n.
[40] Y. Xiu, W. Fan, X. Zhen, Z. Ying, C. Ming, Synthesis of CeO_2 nanoparticles by mechanochemical processing and the inhibiting action of NaCl on particle agglomeration, Mater. Lett. 59 (2005) 48–52, https://doi.org/10.1016/j.matlet.2004.05.089.
[41] R.D. Shannon, Revised effective ionic radii and systematic studies of interatomie distances in halides and chaleogenides, Acta Crystallogr. A 32 (1976) 751–767.
[42] F. Lin, J. Shao, H. Tang, Y. Li, Z. Wang, G. Chen, D. Yuan, K. Cen, Enhancement of NO oxidation activity and SO_2 resistance over $LaMnO_{3+\delta}$ perovskites catalysts with metal substitution and acid treatment, Appl. Surf. Sci. 479 (2019) 234–246, https://doi.org/10.1016/j.apsusc.2019.02.104.
[43] M. V Abrashev, A.P. Litvinchuk, M.N. Iliev, R.L. Meng, V.N. Popov, V.G. Ivanov, R. A. Chakalov, C. Thomsen, Comparative study of optical phonons in the rhombohedrally distorted perovskites $LaAlO_3$ and $LaMnO_3$, Phys. Rev. B 59 (1999) 4146–4153, https://doi.org/10.1103/PhysRevB.59.4146.
[44] J. Topfer, J.B. Goodenough, $LaMnO_{3+\delta}$ revisited, J. Solid State Chem. 130 (1997) 117–128.
[45] C. Ritter, M.R. Ibarra, J.M. De Teresa, P.A. Algarabel, C. Marquina, J. Blasco, J. García, S. Oseroff, S.-W. Cheong, Influence of oxygen content on the structural, magnetotransport, and magnetic properties of $LaMnO_{3+\delta}$, Phys. Rev. B 56 (1997) 8902–8911.
[46] L. Malavasi, C. Ritter, M. Cristina, C. Tealdi, M.S. Islam, C. Bruno, G. Flor, Effects of cation vacancy distribution in doped $LaMnO_{3+\delta}$ perovskites, J. Solid State Chem. 178 (2005) 2042–2049, https://doi.org/10.1016/j.jssc.2005.04.019.
[47] J.A. Alonso, Non-stoichiometry and properties of mixed-valence manganites, Phil. Trans. Roy. Soc. Lond. 356 (1998) 1617–1634, https://doi.org/10.1098/rsta.1998.0238.
[48] Q. Huang, J.W. Lynn, Structure and magnetic order in undoped lanthanum manganite, Phys. Rev. B 55 (1997) 14987–14999.
[49] L. Malavasi, Role of defect chemistry in the properties of perovskite manganites, J. Mater. Chem. 18 (2008) 3295–3308, https://doi.org/10.1039/b800099a.
[50] H. Taguchi, A. Shimizu, M. Nagao, H. Kido, Synthesis and characterization of four-layered hexagonal $(Sr_{1-x}Ba_x)MnO_3$ ($0.0 \leq x \leq 0.5$), J. Ceram. Soc. Japan. 115 (2007) 77–80, https://doi.org/10.2109/jcersj.115.77.
[51] Ulrich Muller, Inorganic Structural Chemistry, second ed., John Wiley & Sons, Chichester, UK, 2006.
[52] R. Laiho, K.G. Lisunov, E. LaLahderanta, P.A. Petrenko, J. Salminen, V.N. Stamov, Y.P. Stepanov, V.S. Zakhvalinskii, Low-field magnetic properties of $LaMnO_{3+\delta}$, J. Phys. Chem. Solid. 64 (2003) 2313–2319, https://doi.org/10.1016/S0022-3697(03)00266-X.
[53] J.A. Alonso, M.J. Martinez-Lope, M.T. Casáis, A. Muiñoz, Magnetic structures of $LaMnO_{3+\delta}$ perovskites ($\delta = 0.11, 0.15, 0.26$), Solid State Commun. 102 (1997) 7–12.
[54] S. Das, P. Roychoudhury, S. De, A. Roy, S. Chatterjee, K. De, Magnetic and electrical transport of the cation-deficient $LaMnO_3$: common origin for both Sr-doping and self-doping effects, Phys. B Condens. Matter 544 (2018) 17–22, https://doi.org/10.1016/j.physb.2018.05.004.
[55] M. Iqbal, M.N. Khan, A.A. Khan, Structural, magnetic, magnetocaloric and critical behavior studies in the vicinity of the paramagnetic to ferromagnetic phase transition temperature in $LaMnO_{3+\delta}$ compound, J. Magn. Magn Mater. 465 (2018) 670–677, https://doi.org/10.1016/j.jmmm.2018.06.026.
[56] C. Papastaikoudis, E. Syskakis, Unusual magnetic properties of $LaMnO_{3+\delta}$, J. Magn. Magn Mater. 276 (2004) 444–445, https://doi.org/10.1016/j.jmmm.2003.11.152.
[57] R. Horyn, A.J. Zaleski, E. Bukowska, A. Sikora, On magnetic properties of $LaMnO_{3\pm\delta}$ phase within its domain, J. Alloys Compd. 383 (2004) 80–84, https://doi.org/10.1016/j.jallcom.2004.04.012.
[58] M.N. Iliev, M.V. Abrashev, Raman phonons and Raman Jahn-Teller bands in perovskite-like manganites, J. Raman Spectrosc. 32 (2001) 805–811, https://doi.org/10.1002/jrs.770.
[59] V.B. Podobedov, A. Weber, D.B. Romero, J.P. Rice, H.D. Drew, Raman scattering in $La_{1-x}Sr_xMnO_3$ single crystals ($x = 0, 0.1, 0.2, 0.3$), Solid State Commun. 105 (1998) 589–593, https://doi.org/10.1016/S0038-1098(97)10185-5.
[60] A. Sacchetti, M. Baldini, P. Postorino, C. Martin, A. Maignan, Raman spectroscopy on cubic and hexagonal $SrMnO_3$, J. Raman Spectrosc. 37 (2006) 591–596, https://doi.org/10.1002/jrs.1484.
[61] J.F. Moulder, W.F. Stickle, P.F. Sobol, B.D. Kenneth, Handbook of X-Ray Photoelectron Spectroscopy, first ed., Perkin-Elmer Corporation, Eden Prairie, 1992.
[62] G. Wulfsberg, Inorganic Chemistry, first ed., Science, University Books, Sausalito, 2000.
[63] A.J. Millis, B.I. Shraiman, R. Mueller, Dynamic Jahn-Teller effect and colossal magnetoresistance in $La_{1-x}Sr_xMnO_3$, Phys. Rev. Lett. 77 (1996) 175–178.
[64] P. Norby, I.G.K. Andersen, E.K. Anderson, The crystal structure of lanthanum manganate (lll), $LaMnO_3$, at room temperature and at 1273 K under N_2, J. Solid State Chem. 119 (1995) 191–196.
[65] K. Kuroda, N. Ishizawa, N. Mizutani, M. Kato, The crystal structure of alfa-$SrMn0_3$, J. Solid State Chem. 38 (1981) 297–299.
[66] D.A. Pawlak, M. Ito, M. Oku, K. Shimamura, T. Fukuda, Interpretation of XPS O (1s) in mixed oxides proved on mixed perovskite crystals, J. Phys. Chem. B 106 (2002) 504–507.
[67] F. Li, Y. Zhan, T. Lee, X. Liu, A. Chikamatsu, T. Guo, H. Lin, J.C.A. Huang, M. Fahlman, Modified surface electronic and magnetic properties of $La_{0.6}Sr_{0.4}MnO_3$ thin films for spintronics applications, J. Phys. Chem. C 115 (2011) 16947–16953.
[68] M.M. Natile, A. Galenda, A. Glisenti, M. Maria, A. Galenda, A. Glisenti, From La_2O_3 to $LaCoO_3$: XPS analysis, Surf. Sci. Spectra 15 (2008) 1–13, https://doi.org/10.1116/11.20061006.
[69] K.A. Stoerzinger, W.T. Hong, E.J. Crumlin, H. Bluhm, M.D. Biegalski, Water reactivity on the $LaCoO_3$ (001) surface: an ambient pressure, J. Phys. Chem. C 118 (2014) 19733–19741, https://doi.org/10.1021/jp502970r.
[70] T. Geng, N. Zhang, Electronic structure of the perovskite oxides $La_{1-x}Sr_xMnO_3$, Phys. Lett. 351 (2006) 314–318.
[71] C. Zener, Interaction between the d-Shells in the Transition Metals. II Ferromagnetic compounds of manganese with perovskite structure, Phys. Rev. 81 (1951) 403–405.
[72] X. Zhou, J. Xue, D. Zhou, Z. Wang, Y. Bai, X. Wu, X. Liu, J. Meng, Mn valence, magnetic, and electrical properties of $LaMnO_{3+\delta}$ nanofibers by electrospinning, ACS Appl. Mater. Interfaces 2 (2010) 2689–2693, https://doi.org/10.1021/am1004738.
[73] V. Markovich, G. Jung, I. Fita, D. Mogilyansky, X. Wu, A. Wisniewski, R. Puzniak, N. Froumin, L. Titelman, L. Vradman, M. Herskowitz, G. Gorodetsky, Magnetotransport in granular $LaMnO_{3+\delta}$ manganite with nano-sized particles, J. Phys. D Appl. Phys. 41 (2008), 185001, https://doi.org/10.1088/0022-3727/41/18/185001.
[74] P.S. Tola, H.S. Kim, D.H. Kim, T.L. Phan, J.S. Rhyee, W.H. Shon, D.S. Yang, D. H. Manh, B.W. Lee, Tunable magnetic properties and magnetocaloric effect of off-stoichiometric $LaMnO_3$ nanoparticles, J. Phys. Chem. Solid. 111 (2017) 219–228, https://doi.org/10.1016/j.jpcs.2017.07.022.
[75] J.S. Z, J.B. Goodenough, Unusual evolution of the magnetic interactions versus structural distortions in $RMnO_3$ perovskites, Phys. Rev. Lett. 96 (2006) 247202.
[76] Y.M. Mukovskii, Anisotropy of magnetic properties in $LaMnO_3$ single crystals, J. Magn. Magn Mater. 272–276 (2004) 98–99, https://doi.org/10.1016/j.jmmm.2003.11.042.
[77] C. Zhou, K. Huang, L. Yuan, W. Feng, X. Chu, Z. Geng, X. Wu, L. Wang, S. Feng, Green catalyst: magnetic $La_{0.7}Sr_{0.3}MnO_3$ hollow microspheres, New J. Chem. 39 (2015) 2413–2416, https://doi.org/10.1039/c4nj01955e.
[78] A. Biswas, S. Chandra, M. Phan, H. Srikanth, Magnetocaloric properties of nanocrystalline $LaMnO_3$: enhancement of refrigerant capacity and relative cooling power, J. Alloys Compd. 545 (2012) 157–161, https://doi.org/10.1016/j.jallcom.2012.08.001.
[79] Y. Wang, T. Ma, C. Wu, M. Yan, C. Zhang, X. Chen, G. Sun, S. Yang, Yu Wang, T. Chang, C. Zhou, X. Liao, X. Zheng, Correlation between magnetostriction and magnetic structure in pseudobinary compounds $Tb(Co_{1-x}Fe_x)_2$, AIP Adv. (2017), 075311, https://doi.org/10.1063/1.4991734.
[80] U. Salazar-kuri, J.O. Estevez, N.R. Silva-gonzález, U. Pal, Large magnetostriction in chemically fabricated $CoFe_2O_4$ nanoparticles and its temperature dependence,

J. Magn. Magn Mater. 460 (2018) 141–145, https://doi.org/10.1016/j.jmmm.2018.03.074.

[81] B.C. Zhao, Y.Q. Ma, W.H. Song, Y.P. Sun, Magnetization steps in the phase separated manganite $La_{0.275}Pr_{0.35}Ca_{0.375}MnO_3$, Phys. Lett. 354 (2006) 472–476, https://doi.org/10.1016/j.physleta.2006.01.088, 354.

[82] C.N. Chinnasamy, A. Narayanasamy, N. Ponpandian, K. Chattopadhyay, K. Shinoda, B. Jeyadevan, K. Tohji, K. Nakatsuka, T. Furubayashi, I. Nakatani, Mixed spinel structure in nanocrystalline $NiFe_2O_4$, Phys. Rev. B 63 (2001) 184108, https://doi.org/10.1103/PhysRevB.63.184108.

[83] P. Kollu, S. Prathapani, E.K. Varaprasadarao, C. Santosh, S. Mallick, N. Grace, D. Bahadur, Anomalous magnetic behavior in nanocomposite materials of reduced graphene oxide-Ni/$NiFe_2O_4$, Appl. Phys. Lett. 105 (2014), 052412, https://doi.org/10.1063/1.4892476.

[84] R. Mahendiran, S.K. Tiwary, A.K. Raychaudhuri, T. V Ramakrishnan, Structure, electron-transport properties, and giant magnetoresistance of hole-doped $LaMnO_3$ systems, Phys. Rev. B 53 (1996) 3348–3358.

[85] D.H. Manh, P.T. Phong, P.H. Nam, D.K. Tung, N.X. Phuc, I. Lee, Structural and magnetic study of $La_{0.7}Sr_{0.3}MnO_3$ nanoparticles and AC magnetic heating characteristics for hyperthermia applications, Physica B 444 (2014) 94–102.

[86] J.B. Goodenough, Localized to itinerant electronic transition in perovskite oxides, in: Structure and Bonding, first ed., Springer, Berlin, 2001.